Journal Pre-proof

Mitochondria-targeting nanomedicine self-assembled from GSH-responsive paclitaxel-ss-berberine conjugate for synergetic cancer treatment with enhanced cytotoxicity

Yu Cheng, Yuanhui Ji

PII: S0168-3659(19)30729-1

DOI: https://doi.org/10.1016/j.jconrel.2019.12.011

Reference: COREL 10054

To appear in: *Journal of Controlled Release*

Received date: 22 September 2019

Revised date: 3 December 2019

Accepted date: 9 December 2019

Please cite this article as: Y. Cheng and Y. Ji, Mitochondria-targeting nanomedicine self-assembled from GSH-responsive paclitaxel-ss-berberine conjugate for synergetic cancer treatment with enhanced cytotoxicity, *Journal of Controlled Release* (2019), https://doi.org/10.1016/j.jconrel.2019.12.011

Mitochondria-targeting nanomedicine self-assembled from GSH-responsive paclitaxel-ss-berberine conjugate for synergetic cancer treatment with enhanced cytotoxicity

Yu Cheng, Yuanhui Ji*

Jiangsu Province Hi-Tech Key Laboratory for Biomedical Research, School of Chemistry and Chemical Engineering, Southeast University, Nanjing, 211189, P.R. China

* Corresponding author: Tel: +86-13951907361; Email: yuanhui.ji@seu.edu.cn; yuanhuijinj@163.com.

Abstract:

Mitochondria play a fundamental role in plenty of cellular metabolic processes, and mitochondria-homing drug delivery is a promising and effective strategy for cancer treatment. Paclitaxel (PTX) is a broad-spectrum anticancer drug, but its therapeutic effect is highly limited due to the development of multidrug resistance. Berberine (BBR) can selectively accumulate in tumor cell mitochondria and inhibit the growth of cancer cells with different biological action mechanism from PTX. Here, these two "old" drug molecules, BBR and PTX were linked together by a disulfide bond rope to construct GSH-responsible drug-drug conjugate (PTX-ss-BBR). Molecular dynamics simulation results revealed that PTX-ss-BBR conjugate could be self-assembled in water to form nanoparticles (PTX-ss-BBR NPs) forced by π-π stacking and hydrophobic interactions and the average size of NPs was around 165 nm measured by DLS. The better *in vitro* potency of PTX-ss-BBR NPs against A549 cells might be ascribed to the simultaneous drug release and mitochondria-targeting delivery, which dissipated mitochondria membrane potential, upregulated ROS levels in cancer cells, arrested cells in phase G2/M, elicited apoptosis of cancer cells and inhibited the growth of tumors. Furthermore, PTX-ss-BBR NPs also exerted efficacy better than or comparable to BBR on *S. aureus* and *E. coli*, which were closely associated with the development of lung cancer. The synergistic effect of PTX and BBR enhanced the treatment effect of conventional chemotherapy drugs against A549 cells.

Keywords: Paclitaxel, berberine, mitochondria-targeting, self-assembled nanomedicine

1. Introduction

Cancer is the primary cause of disease-related mortality all over the world. Therefore, scientists and researchers spare no efforts to finding better approaches and solutions to fight against cancer [1]. In the middle of varieties of treatment approaches of cancer, chemotherapeutics remains an obbligato method. Paclitaxel (PTX), a broad-spectrum anticancer drug acting on microtubule and many of its nano-formulations have been successfully employed in clinical therapy of ovarian cancer, lung cancer, breast cancer, and so on [2,3]. However, the occurrence of multidrug

resistance (MDR) has severely limited the clinical usage of PTX [4]. A leading cause of MDR development is that therapeutic drugs are pumped out by power-dependent efflux pump from the cancer cells, which is obligate in the lower accumulation of drug in the cells and failed treatment outcome [5]. Cellular energy production is mainly derived from aerobic metabolism in the mitochondria, which play critical roles in configuring the apoptosis pathway for cancer cells [6]. Some reports have also found that PTX exerts a direct effect on mitochondria of cancer cells, rendering the apoptosis of cancer cells [7-9]. Therefore, homing delivery of therapeutic drugs to the mitochondria from cancer cells is a hopeful solution to diminish MDR in tumor chemotherapy.

Among mitochondria-targeting approaches, delocalized lipophilic cations (DLCs) are the most fashionable chemicals such as triphenylphosphonium, mitochondria-penetrating peptides which are usually conjugated to small molecules or decorated on the surface of drug delivery platforms [10,11]. Due to more negative charged mitochondrial membrane potentials, DLCs are more likely to accumulate in the mitochondria of tumor cells than normal cells. These drug delivery platforms offer preferential mitochondrial accumulation and enhanced drug uptake [12]. Berberine (BBR) is an isoquinoline alkaloid with plenty of prominent pharmacological effects including antimicrobial [13], antiviral [14], antidiabetic [15], anti-inflammatory[16] and anticancer [17] activities. Strikingly, BBR can selectively accumulate into the mitochondria in cancer cells, which may be put down to its amphiphilic structure and delocalized positive charge [18-21]. Moreover, cancer cell apoptosis induced by BBR acting on mitochondria has been confirmed with the deep mechanisms interpreted as dissipating the mitochondrial membrane potential, upregulating ROS levels, inducing changes in permeability of mitochondrial membrane [17,18].

Nanomedicine delivery systems such as micelles [22], inorganic materials [23,24], liposomes [25,26], vesicles [27] and dendrimers [28], have been immensely investigated in order to elevate the physio-chemical properties and efficacy of therapeutic drugs. In the midst of the nanomedicine delivery platforms, nanodrugs formed by small molecule self-assembly have shown great potential for their high drug loading and reduced side effects without usage of drug carriers [29,30]. Besides, the nanosystems are able to deliver drugs to the tumor sites by making use of the enhanced permeability and retention (EPR) effect [31]. Glutathione (GSH) is a strong biological reducing tripeptide and is as commonly used stimuli factors for disulfide bond at certain concentration [32]. The mitochondria in cancer cells express a higher level of GSH than that in the normal tissue (varying between 2 and 10 $\mu mol \cdot L^{-1}$), enough to reduce the disulfide bond [33]. Therefore, mitochondria-targeting GSH-sensitive drug delivery platform is expected to enhance the effect of chemotherapy.

Taking above observations into account, considering the excellent mitochondria-targeting feature and potential synergetic anticancer effect of BBR and the clinically outstanding contribution of PTX, we described herein a new GSH-responsive conjugate, which was

constructed through a disulfide bond spacer to connect paclitaxel with berberine. Scheme 1 illustrated the structure and synthetic routes of the mitochondria-targeting paclitaxel-ss-berberine (PTX-ss-BBR) conjugate, which was able to form unanimous nanoparticles (PTX-ss-BBR NPs). Based on the aforementioned advantages, the NPs announced better *in vitro* potency on A549 cells due to the simultaneous drug release and mitochondria-targeting drug delivery.

2. Materials and methods

2.1. Materials

Berberine hydrochloride, paclitaxel, methanol (CH_3OH), acetonitrile (CH_3CN) and glutathione (GSH) were provided by Shanghai Adamas Reagent Co., Ltd. (Shanghai, China). 4-Dimethylaminopyridine (DMAP), 3,3-dithiodipropionic acid and *N,N*-Dicyclohexylcarbodiimide (DCC) were obtained from Nanjing Juyou Scientific Equipment Co., Ltd. (Nanjing, China). 3-(4,5-Dimethyl-2-tetrazolyl)-2,5-diphenyltetrazolium bromide (MTT) chloroform (CH_3Cl_3) were purchased from Nanjing Wanqing Chemical Glassware Istrument Co., Ltd. (Nanjing, China). Mitotracker Red was purchased from Jiangsu KeyGEN Biotech Co., Ltd. (Nanjing, China). Other reagents were provided by local commercial suppliers.

2.2. Chemistry synthesis of GSH-responsive PTX-ss-BBR conjugate

Synthesis of Compound **2**: Berberine hydrochloride (5.0 g, 13.47 mmol) in vacuo was stirred at 190 ^{o}C for 60 minutes to obtain crude product, which was purified *via* column chromatography on silica gel (eluent: chloroform/methanol = 9/1, V/V) to produce compound **2** (3.68 g) as red-brown solid with 85% yield.

Synthesis of Compound **3**: Intermediate **2** (4.22 g, 13.14 mmol) and K_2CO_3 (1.81 g, 13.14 mmol) in CH_3CN (18 mL) were reacted at 50 ^{o}C for 30 minutes. 2-Bromoethanol (1.65 g, 13.14 mmol) was added to the mixed system, and subsequently the reacted temperature was gradually heated to 82 ^{o}C and went on for 24 h. After the end of the reaction, the temperature was decreased to 25 ^{o}C slowly, and the remaining CH_3CN was evaporated by rotary evaporation method. The condensed solution was purified *via* column chromatography on silica gel (eluent: chloroform/methanol = 9/1, V/V) to produce compound **3** (5.03 g) as yellow solid with 86% yield. ^{1}H NMR (600 MHz, MeOD+$CDCl_3$) δ 9.95 (s, 1H), 8.62 (s, 1H), 8.05 (d, *J* = 9.1 Hz, 1H), 8.00 (d, *J* = 9.0 Hz, 1H), 7.59 (s, 1H), 6.93 (s, 1H), 6.13 (s, 2H), 4.99–4.93 (m, 2H), 4.54–4.50 (m, 2H), 4.12 (s, 3H), 4.00–3.96 (m, 2H), 3.31–3.26 (m, 2H). HRMS (ESI) calcd. for $C_{21}H_{20}NO_5$ $[M\text{-}Br]^{+}$, 366.1336; found, 366.13315.

Synthesis of Compound **4**: Berberine derivative **3** (4.48 g, 10.11 mmol) was refluxed in CH_3OH (35 mL) for a quarter, then sodium borohydride (1.15 g, 30.33 mmol) was added to the solution

little by little accompanied by vigorous stirring at 0 ^{o}C. Twelve hours later, the CH_3OH was evaporated by rotary evaporation method. The condensed solution was purified *via* column chromatography on silica gel (eluent: methanol/chloroform = 1/50, V/V) to obtain compound **4** (3.06 g) as light yellow solid with 57% yield. ^{1}H NMR (600 MHz, $CDCl_3$) δ 6.88 (d, *J* = 8.4 Hz, 1H), 6.79 (d, *J* = 8.4 Hz, 1H), 6.72 (s, 1H), 6.59 (s, 1H), 5.91 (s, 2H), 4.26 (d, *J* = 15.5 Hz, 1H), 4.16–4.12 (m, 1H), 4.04 (dd, *J* = 10.3, 5.8 Hz, 1H), 3.88–3.81 (m, 5H), 3.57–3.51 (m, 2H), 3.22 (dd, *J* = 15.9, 3.3 Hz, 1H), 3.17 (dd, *J* = 10.4, 4.7 Hz, 1H), 3.10 (d, *J* = 11.2 Hz, 1H), 2.82 (dd, *J* = 15.5, 11.6 Hz, 1H), 2.63 (dd, *J* = 21.8, 10.6 Hz, 2H).; HRMS (ESI) calcd. for $C_{21}H_{23}NO_5$ $[M+H]^+$, 370.1654; found, 370.16589.

Synthesis of Compound **5**: The 20 mL pyridine liquid including tetrahydroberberine **4** (3 g, 8.13 mmol) was added to the mixture system of DMAP (98.95 mg, 0.81 mmol), DCC (2.52 g, 12.14 mmol), 3,3'-dithiodipropionic acid (1.71 g, 8.13 mmol) in pyridine under dry N_2, and the mixted system was reacted at 0 °C for 48 h. Then, residual pyridine was evaporated by rotary evaporation method. The condensed solution was purified by column chromatography on silica gel (eluent: methanol/chloroform = 1/20, V/V) and dried under vacuo, obtaining the pure compound **5** (2.87 g) as light yellow solid with 63% yield. ^{1}H NMR (600 MHz, MeOD) δ 7.03 (s, 2H), 6.91 (s, 1H), 6.71 (s, 1H), 5.96 (s, 2H), 4.47 (s, 1H), 4.42–4.37 (m, 2H), 4.35–4.30 (m, 2H), 3.86 (d, *J* = 3.7 Hz, 3H), 3.72 (s, 1H), 3.64 (dd, *J* = 17.0, 4.3 Hz, 1H), 3.37 (s, 1H), 3.22 (s, 1H), 3.11–3.09 (m, 1H), 3.07–2.99 (m, 2H), 2.96 (dd, *J* = 13.5, 6.2 Hz, 4H), 2.82 (t, *J* = 6.9 Hz, 2H), 2.66 (t, *J* = 7.0 Hz, 2H), 2.59 (t, *J* = 6.1 Hz, 1H).; HRMS (ESI) calcd. for $C_{27}H_{31}NO_8S_2$ $[M+H]^+$, 562.1569; found, 562.15688.

Synthesis of Compound **6**: The 20 mL pyridine liquid including paclitaxel (2.0 g, 2.34 mmol) was added little by little to the mixture system of DCC (724.22 mg, 3.51 mmol), compound **5** (1.31 g, 2.34 mmol), DMAP (28.09 mg, 0.23 mmol) in pyridine under dry N_2, and the mixted system was reacted at 0 °C for 48 h. Then, the residual pyridine was evaporated by rotary evaporation method. The condensed solution was purified *via* column chromatography on silica gel (eluent: methanol/chloroform = 1/50, V/V) and dried under vacuo, obtaining the pure compound **6** (2.78 g) as light yellow solid with 85% yield. IR (KBr) ν: 3448, 2944, 1727, 1666, 1484, 1452, 1373, 1240, 1074, 979, 707. ^{1}H NMR (600 MHz, $CDCl_3$) δ 8.14 (d, *J* = 7.6 Hz, 2H), 7.75 (d, *J* = 7.2 Hz, 2H), 7.61 (t, *J* = 7.4 Hz, 1H), 7.55–7.48 (m, 3H), 7.44–7.37 (m, 6H), 7.34 (d, *J* = 7.5 Hz, 1H), 7.06 (s, 1H), 6.87 (d, *J* = 8.4 Hz, 1H), 6.78 (d, *J* = 8.3 Hz, 1H), 6.72 (s, 1H), 6.58 (d, *J* = 6.5 Hz, 1H), 6.29 (s, 1H), 6.24 (t, *J* = 8.7 Hz, 1H), 5.98 (d, *J* = 9.0 Hz, 1H), 5.91 (s, 2H), 5.68 (d, *J* = 7.1 Hz, 1H), 5.53 (s, 1H), 4.97 (d, *J* = 9.0 Hz, 1H), 4.44 (t, *J* = 8.5 Hz, 1H), 4.38 (t, *J* = 9.4 Hz, 2H), 4.32 (d, *J* = 8.5 Hz, 1H), 4.26 (dd, *J* = 17.7, 14.3 Hz, 2H), 4.22–4.16 (m, 2H), 3.81 (d, *J* = 10.5 Hz, 4H), 3.51 (s, 2H), 3.22 (d, *J* = 15.0 Hz, 1H), 3.12 (d, *J* = 24.4 Hz, 2H), 2.91 (t, *J* = 7.0

Hz, 2H), 2.87 (d, *J* = 5.1 Hz, 2H), 2.85–2.75 (m, 4H), 2.65 (d, *J* = 14.5 Hz, 2H), 2.54 (d, *J* = 14.7 Hz, 2H), 2.45 (s, 3H), 2.40–2.33 (m, 1H), 2.22 (s, 3H), 2.19–2.13 (m, 1H), 1.94 (s, 3H), 1.91–1.81 (m, 2H), 1.68 (s, 3H), 1.23 (s, 3H), 1.13 (s, 3H).; HRMS (ESI) calcd. for $C_{74}H_{80}N_2O_{21}S_2$ $[M+H]^+$, 1397.4773; found, 1397.47749.

Synthesis of PTX-ss-BBR conjugate **7**: NBS (86.49 mg, 0.48 mmol) was added little by little to the solution of compound **6** (450 mg, 0.32 mmol) in $CHCl_3$ (10 mL), and reacted at 50 ^oC for 6 h. The reaction solution was decreased to 25 ^oC and then filtered. The condensed solution was purified *via* column chromatography on silica gel (eluent: chloroform/methanol = 9/1, V/V) and dried under vacuum, obtaining the pure compound **7** (133.57 mg) as yellow solid with 45% yield. IR (KBr) ν: 3421, 2935, 1739, 1637, 1600, 1502, 1450, 1390, 1316, 1240, 1074, 927, 711. ^1H NMR (600 MHz, CD_3OD, ppm): δ 9.75 (s, 1H), 8.70 (s, 1H), 8.10 (d, *J* = 8.4 Hz, 3H), 8.00 (d, *J* = 9.1 Hz, 1H), 7.79 (d, *J* = 8.5 Hz, 2H), 7.67 (d, *J* = 8.6 Hz, 1H), 7.65 (s, 1H), 7.60 (d, *J* = 7.9 Hz, 2H), 7.52 (d, *J* = 7.5 Hz, 1H), 7.47–7.43 (m, 6H), 7.26 (t, *J* = 7.2 Hz, 1H), 6.94 (s, 1H), 6.40 (s, 1H), 6.10 (s, 2H), 6.01 (d, *J* = 10.1 Hz, 1H), 5.78 (d, *J* = 6.8 Hz, 1H), 5.61 (d, *J* = 7.2 Hz, 1H), 5.46 (d, *J* = 6.7 Hz, 1H), 4.97 (d, *J* = 7.9 Hz, 1H), 4.94–4.91 (m, 2H), 4.67 (t, *J* = 4.0 Hz, 2H), 4.56 (d, *J* = 8.2 Hz, 2H), 4.29 (d, *J* = 11.0 Hz, 1H), 4.16 (s, 2H), 4.10 (s, 3H), 3.76 (d, *J* = 7.2 Hz, 1H), 3.27 – 3.24 (m, 2H), 2.86 (d, *J* = 6.3 Hz, 2H), 2.81 (dd, *J* = 14.5, 8.1 Hz, 4H), 2.67 (t, *J* = 6.8 Hz, 2H), 2.37 (s, 3H), 2.13 (s, 3H), 1.87 (s, 3H), 1.76 (dd, *J* = 14.6, 4.6 Hz, 2H), 1.63 (s, 3H), 1.28 (s, 3H), 1.12 (s, 3H), 1.09 (s, 3H), 0.90 (t, *J* = 7.0 Hz, 1H).; HRMS (ESI) calcd. for $C_{74}H_{77}N_2O_{21}S_2$ $[M-Br]^+$, 1393.4455; found, 1393.44153.

^1H NMR spectra were recorded on a Bruker AVANCE III HD NMR spectrometer operating at 600 MHz and using deuterated chloroform ($CDCl_3$) or methanol (CD_3OD) as solvent. The high resolution mass spectra (HRMS) were recorded on a Bruker solanX 70 FT-MS with ESI resource. FT-IR spectra were carried out on Bruker RFS100/S spectrophotometer (Bio-Rad, Cambridge, MA, USA) using KBr pellets in the 400-4000 cm^{-1} range.

2.3. Preparation and characterization of PTX-ss-BBR NPs

PTX-ss-BBR NPs were prepared from the nano-precipitation method. The PTX-ss-BBR conjugate (10 mg) was dissolved in DMSO (0.5 mL), followed by ultrasound about 5 min and the solution was injected gradually into the 20 mL deionized water to form the nanomedicine. After that, the resulting nanoparticles were dialyzed (MWCO = 2000 Da) against deionized water for 48 h for complete removal of the DMSO and unbond compounds.

The morphological observation of the PTX-ss-BBR NPs was checked by the TEM (JEM-2100F, JEOL). The size and size distribution of the NPs was detected by DLS (Malvern Zetasizer Nano-ZS90, Malvern). The light scattering intensities (Kcps) of acquous solutions containing

varying concentration PTX-ss-BBR conjugates were measured on DLS analyzer, and then plot over the concentration (log scale) of PTX-ss-BBR to determine the critical micelle concentration.

2.4. In vitro drug release

The *in vitro* drug release activity of PTX-ss-BBR NPs was evaluated by using a typical dialysis strategy. Briefly, 1 mL of NPs solution was placed in the dialysis bag (MWCO = 2000 Da) and immersed in 30 mL buffer solution (pH = 7.4, with or without 10 mM GSH) containing 1% (v/v) Tween 80 with continuously shaking at a ratio of 100 rpm and keeping at 37 °C. At set time points, 2 mL release medium were taken out for fluorescence measurement and an equal amount of fresh PBS was used to replace the release medium. A fluoromax 4 spectrofluorometer (HORIBA, USA) (excitation at 370 nm) was employed for measuring the amount of released BBR.

2.5. Cell culture.

A549 cell is a human lung adenocarcinoma cell line, HeLa cell is a cervical cancer cell line and HepG2 cell is a human hepatoma cell line, which is received from China Pharmaceutical University (Nanjing, China). All cells were cultured in RPMI 1640 or DMEM medium complemented with 100 μg/mL streptomycin, 10% FBS, 100 U/mL penicillin and 100 μg/mL streptomycin in a humidified incubator at 5% CO_2, 37 °C.

2.6. Cell viability assay.

The MTT assay was employed to detect the *in vitro* cytotoxicity of PTX-ss-BBR NPs and PTX against A549, HeLa and HepG2 cells. The 96-well plates (1×10^4 cells per well) were used to seed various cells and kept overnight. Following the attachment of cells, fresh culture medium containing PTX-ss-BBR NPs and PTX were added at tested concentrations of 0.625, 1.25, 2.5, 5, 10, 20 and 40 μM and incubation time was set 24 h and 48 h. After washing twice, 25 μL 5% MTT stock solution was added and continued to incubate for another 4 h. The 150 μL dimethyl sulfoxide solvent was used to dissolve generated formazan precipitate and the absorbance intensity at 570 nm of each sample measured by microplate-680 reader (Bio-Rad, CA). Cell viability (%) of experimental groups against the different cells was determined and untreated cells as the control group. Each group was performed in parallel three times and GraphPad Prism software was employed for calculating the half-maximal inhibitory concentration (IC_{50}) value.

2.7. Mitochondrial targeting

Laser confocal scanning microscope (CLSM) was used to observe the mitochondrial localization of BBR and PTX-ss-BBR NPs in A549 cells. The glass-bottomed dish (1×10^4 cells per dish) were used to seed A549 cells for 12 h at 5% CO_2 and 37 ^oC and cultured with 5 μM BBR or PTX-ss-BBR NPs for another 60 or 120 minutes under the same culture conditions. After

treatment, the A549 cells were washed 3 times with 2 ml of buffer solution in dark conditions, and then the A549 cells were stained with mitochondrial localization reagent Mitotracker Red (1 μM) and cultured for 25 minutes under the same culture conditions. After the completion of the culture, the cells were washed again by using 2 ml of the buffer solution three times, and then the fluorescence of the cells was observed by CLSM.

2.8. Mitochondrial membrance potential

The JC-1 (Jiangsu KeyGEN, Nanjing, China), a fluorescent dye was used to measure the change of mitochondrial membrance potential (Δψm). The 6-well plates (1×10^5 cells per dish) were used to seed A549 cells for 12 h at 5% CO_2 and 37 ^oC and cultured with 5 μM BBR or PTX-ss-BBR NPs for another 48 h under the same culture conditions. After treatment, the A549 cells were washed 3 times with 2 ml of buffer solution in dark conditions, and then the A549 cells were stained with 0.5 mL of 5 μg/mL JC-1 and cultured for a quarter under the same culture conditions. After the completion of the culture, the cells were washed again by using 2 ml of the buffer solution three times before analysis by FACScan flow cytometer.

2.9. ROS detection assay

The intracellular production of ROS induced by different groups was measured using a 2',7'-dichlorodihydrofluorescein diacetate (DCFH-DA) kit (Jiangsu KeyGEN, Nanjing, China). The 6-well plates (1×10^5 cells per dish) were used to seed A549 cells for 12 h at 5% CO_2 and 37 ^oC and cultured with 5 μM BBR or PTX-ss-BBR NPs for another 48 h under the same culture conditions. After treatment, the A549 cells were washed 3 times with 2 ml of buffer solution in dark conditions, and then the A549 cells were stained with 0.5 mL of 20 μM DCFH-DA and cultured for 60 minutes under the same culture conditions. After the completion of the culture, the cells were washed again by using 2 ml of the buffer solution three times before detection of dichlorofluorescein (DCF) by FACScan flow cytometer.

2.10. Apoptosis effect in vitro

The cell apoptosis effect of tested groups was measured using Annexin V-FITC/PI apoptosis detection kit (Jiangsu KeyGEN, Nanjing, China). The 6-well plates (1×10^5 cells per dish) were used to seed A549 cells for 12 h at 5% CO_2 and 37 ^oC and cultured with 5 μM BBR or PTX-ss-BBR NPs for another 48 h under the same culture conditions. After treatment, the A549 cells were washed 3 times with 2 ml of buffer solution in dark conditions, and then the A549 cells were stained with 5 μL iodide and 5 μL Annexin V-FITC and cultured for 30 minutes under the same culture conditions. After the completion of the culture, the cells were washed again by using 2 ml of the buffer solution three times before analysis by FACScan flow cytometer.

2.11. Cell-cycle analysis

The 6-well plates (1×10^5 cells per dish) were used to seed A549 cells for 12 h at 5% CO_2 and 37 ^oC and cultured with 5 μM BBR or PTX-ss-BBR NPs for another 48 h under the same culture conditions. After treatment, the A549 cells were washed 3 times with 2 ml of buffer solution in dark conditions, and then the A549 cells were resuspended in buffer solution with 50 μg/mL PI and 50 μg/mL RNase A. and cultured for 30 minutes under the same culture conditions. After the completion of the culture, the cells were washed again by using 2 ml of the buffer solution three times before analysis by FACScan flow cytometer.

2.12. Statistical analysis

All data are presented as the average ± standard deviation (SD, n = 3). One-way ANOVA analysis by GraphPad Prism software was employed for the analysis of statistical significance.

3. Results

3.1. Chemistry synthesis of GSH-responsive PTX-ss-BBR conjugate

The target PTX-ss-BBR conjugate **7** was synthesized *via* multi-step reactions from commercially available berberine, bromoethanol, 3,3´-dithiodipropionic acid, paclitaxel. The synthetic process was presented in Scheme 1. Compound **2** was easily obtained by selective 9-position demethylation of berberine at 190 ^oC under vacuo for 60 minutes. Berberine intermediate **2** was ulteriorly reacted with bromoethanol through nucleophilic substitution in CH_3CN under reflux to gain compound **3** in 86 % yield, which was reduced by $NaBH_4$ in methanol to produce compound **4** in 57 % yield. The key intermediate **5** was obtained *via* the condensation reaction of compound **4** and 3,3´-dithiodipropionic acid in pyridine with DMAP and DCC. Compound **6** was obtained by a condensation reaction of compound **5** and PTX in pyridine with DMAP and DCC. The target paclitaxel-berberine conjugate **7** was obtained in 28 % yield by the oxidation of compound **6** with NBS in $CHCl_3$ at 50 ^oC for 6 h. Targeted conjugate PTX-ss-BBR and intermediates were confirmed by ^1H NMR, and HRMS spectra.

Scheme 1

Reagents and conditions: i) 190 ^oC/vacuo; ii) K_2CO_3, CH_3CN, bromoethanol, reflux, 24 h; iii) $NaBH_4$, CH_3OH, 0 ^oC; iv) 3,3´-dithiodipropionic acid, pyridine, DMAP, DCC, 0 ^oC, 48 h; v) PTX, pyridine, DCC, 0 ^oC; vi) NBS, $CHCl_3$, 50 ^oC.

Scheme 1. Synthetic route of GSH-responsive PTX-ss-BBR conjugate.

3.2. Characterization of PTX-ss-BBR NPs

The TEM and DLS were used to observe and characterize the morphology and size distribution of PTX-ss-BBR NPs. TEM image demonstrated that the PTX-ss-BBR NPs showed a spherical structure with the size of approximately 150 nm (Fig. 1A). The DLS analysis suggested that

PTX-ss-BBR NPs exhibited a mean diameter of 165.8 ± 2.597 nm (Fig. 1C) with a narrow polydispersity index (PDI = 0.115) and showed a small critical micelle concentration (CMC = 1.26 μM) of PTX-ss-BBR conjugates (Fig. 1F). The diameter measured by DLS remained unvaried over 3 days, suggesting excellent stability of PTX-ss-BBR NPs in PBS and in PBS including 10% fetal bovine serum (FBS, Fig. 1D). The reducing agent-induced dissociation of disulfide bonds in PTX-ss-BBR NPs was monitored by TEM in the presence of 10 mM GSH for 6 h (Fig. 1B).

Figure 1

Fig. 1. (A) TEM image of PTX-ss-BBR NPs. (B) TEM image of PTX-ss-BBR NPs treated with 10 mM GSH for 6h. (C) Particle size of PTX-ss-BBR NPs. (D) Changes of diameter of PTX-ss-BBR nanoparticles in PBS or in PBS and FBS for 3 days. (E) *In virto* release kinetics of drug from NPs in pH 7.4 PBS with or without GSH. (F) The light scattering intensities (Kcps) of acquous solutions containing varying concentration PTX-ss-BBR conjugates.

3.3. Self-assembly mechanism of PTX-ss-BBR conjugate

Computer simulation provides another way to evaluate the self-assembly process of complex systems [34]. To unravel the self-assembly principle of the PTX-ss-BBR conjugate, molecular dynamics (MD) simulations for conjugates were performed in water environment. As shown in Fig. 2, ten PTX-ss-BBR conjugates gathered quickly and uniformly to form a cluster of multimer. After the end of self-assembly, the whole nanocluster's position varied, but remained aggregated together. Noncovalent hydrophobic interactions and π-π stacking accounted for the self-assembly of the ten PTX-ss-BBR conjugates because PTX moieties with multiple phenyl fragments (green color) were in the internal part of the cluster and the more polar BBR fragments (pink color) surrounded the internal part and were exposed to the water media. Furthermore, it was observed that in the first 50ns of the simulation the solvent accessible surface area and the number of hydrogen bonds (Fig. 3A) between the cluster and water were reduced gradually, which announced that the complex system was formed gradually. After longer simulation times, the cluster was apt to keep stable. When the solvation free energy is a negative value, the solvation will be thermodynamically favorable [35]. In this research (Fig. 3B), the solvation free energy was always a negative value and it gradually increased in the first 50 ns. After then, it remained almost unchanged, which indicated that the intermolecular and intramolecular interactions of conjugates contributed more to the formation of nanosystems than spontaneous solvation.

Figure 2

Fig. 2. The supramolecular assembly process of PTX-ss-BBR conjugate in water by MD simulations.

Figure 3

Fig. 3. (A) The solvent accessible surface areas of the assembled nanostructures and the number of hydrogen bonds between the cluster and water. (B) Solvation free energy of assembled nanostructures.

3.4. In vitro drug release of PTX-ss-BBR NPs

The mitochondria in cancer cells express a drastically higher content of GSH than that in the normal environment, enough to reduce the disulfide bond [36]. BBR and PTX were linked together by a disulfide bond rope, which made PTX-ss-BBR NPs liable to disassembly by reducing agent and the nanosystems could be employed as a GSH-responsible drug delivery platform for stimulating release of the drugs in cancer cells. To estimate the GSH sensitivity, the *in vitro* release kinetics of the drugs from PTX-ss-BBR NPs was checked by a typical dialysis method in PBS (pH = 7.4, with 10 mM GSH) or PBS (pH = 7.4, without GSH), simulating the reductive environment of cytoplasm of tumor cells and normal physiological environment, respectively. Here, the accumulative amount of BBR released from PTX-ss-BBR NPs was studied since both BBR and PTX will release simultaneously. According to Fig. 1E, the PTX-ss-BBR NPs was GSH-sensitive and cumulative release amount of BBR was $\approx$ 55% after 10 h treatment at 37 ^{o}C. Only approximately 7% BBR released from PTX-ss-BBR NPs in normal physiological environment over a period of 55 h, which was due to dynamic thermodynamic equilibrium between free PTX-ss-BBR monomer and self-assembled NPs. These release results suggested that the PTX-ss-BBR NPs were as-expectedly minimal drug release in blood circulation and could instantly disassembly and release drugs in a highly reductive microenvironment.

3.5. In vitro anti-tumor efficacy of PTX-ss-BBR NPs

In vitro anticancer activity of PTX-ss-BBR NPs against A549, HeLa and HepG2 cells were studied using MTT assays and the cell viability details and IC_{50} values were presented in Table 1 and Fig. 4, respectively. Free PTX and BBR were chosen as positive control. As shown in Fig. 4, anticancer activity was enhanced with increasing PTX-ss-BBR NPs concentrations and extending treatment time, suggesting that the anticancer efficacy of PTX-ss-BBR NPs was concentration- and time-dependent. BBR exhibited moderate anticancer activity on all cells tested after 48 h treatment. Fig. 4A and B disclosed that self-assembled NPs showed considerably higher anticancer activity on A549 cells than the free PTX, especially after 48 h treatment, the inhibition activity of PTX-ss-BBR NPs (IC_{50} = 0.243 μM) increased by approximately 22% compared to PTX (IC_{50} = 0.31 μM), which might be reasonably interpreted by the fast disassembly of the NPs under reductive tumor microenvironment and the promotion of mitochondria-targeting of drug delivery. While the inhibition efficacy of NPs against HeLa cells was weaker than PTX after 24 h incubation, the anti-tumor activity of NPs (IC_{50} = 1.512 μM) was better than PTX (IC_{50} = 1.653 μM) after 48 h incubation, which might be due to the effective release of the PTX-ss-BBR NPs

after a longer incubation period in HeLa cells. In contrast, HepG2 cells seemed to be less sensitive to PTX-ss-BBR NPs, the IC_{50} values of NPs on HepG2 were higher than PTX after either 24 or 48 h incubation.

Figure 4

Fig. 4. *In vitro* anticancer activity of self-assembled PTX-ss-BBR NPs, PTX and BBR against A549 cells for 24h (A) or 48h (B), HeLa cells for 24h (C) or 48h (D), HepG2 cells for 24h (E) or 48h (F). Data are presented as the mean ± SD (n=3). $^{*}P < 0.05$ *vs.* PTX; $^{\#}P < 0.05$ *vs.* BBR; $^{\#\#}P < 0.01$ *vs.* BBR; $^{\#\#\#}P < 0.001$ *vs.* BBR.

Table 1 IC_{50} values of free BBR, PTX and PTX-SS-BBR NPs on A549, HeLa and HepG2 cells at different times.

Table 1

3.6. In vitro antibacterial efficacy of PTX-ss-BBR NPs

The formation and development of cancer, especially for lung cancer is closely related to bacterial infections, which occurs in up to 70% lung cancer patients and markedly influence the clinical outcome and patient survival [37]. In particular, *Escherichia coli* (*E. coli*), *Staphylococcus aureus* (*S. aureus*) and *Streptococcus pneumoniae* (*S. pneumoniae*) are the most common in lung cancer [38]. Therefore, we evaluated the efficacy of PTX-ss-BBR NPs above three bacteria and berberine as the control group (Table 2). Albeit the NPs exhibited weak activity against *S. pneumoniae* than BBR, it could effectively repress the growth of *S. aureus* (minimal inhibitory concentration (MIC) = 4 μM) and the inhibition ability was twice that of BBR. Moreover, PTX-ss-BBR NPs exhibited an anti-*E. coli* activity comparable to that of BBR with the MIC value of 8 μM.

Table 2 *In vitro* antibacterial activity data as MIC (μM) for PTX-ss-BBR NPs and BBR against *S. aureus*, *S. pneumoniae* and *E. coli*.

Table 2

3.7. Apoptosis-inducing effect in vitro by PTX-ss-BBR NPs

In order to check the apoptosis effect of PTX-ss-BBR NPs, a quantitative annexin V-FITC/PI staining experiment was performed. In Fig. 5, the total apoptotic ratio (early and late apoptosis) in A549 cells after incubation by PTX-ss-BBR NPs was 48.46%, which was much higher than free BBR with 22.07% apoptotic ratio and free PTX with 32.23% apoptotic ratio, respectively. The substantially elevated apoptosis-inducing effect of the PTX-ss-BBR NPs could be a result of the accumulated amount of intracellular BBR and PTX, and the activation of mitochondria-based apoptotic pathway.

Figure 5

Fig. 5. (A) *In vitro* apoptosis analysis against A549 cells treated by BBR, PTX-ss-BBR NPs, and PTX and analyzed by Annexin-v-FITC/PI double staining method. (B) Quantitative ratio of apoptosis. Data are presented as the mean ± SD (n=3). $^{###}P < 0.001$ *vs.* Control; $^{□□□□}P < 0.001$ *vs.* BBR; $^{***}P < 0.001$ *vs.* PTX.

3.8. Cell cycle analysis of A549

A549 cells were harvested with BBR, PTX-ss-BBR NPs and PTX and the untreated cells served as control group. As seen in Fig. 6, BBR, PTX-ss-BBR NPs and PTX induced notable cell-cycle interference in A549. A remarkable decrease in the phase of G0/G1 cells was noticed from 42.90 % (control) to 37.56 %, 29.81 % (lower 30.5% than control), and 32.02 %, while a great increase in G2/M phase of cells was observed from 16.76 % (control) to 23.24 %, 30.84 % (higher 84.1% than control) and 26.07 %, after 48 h exposure to BBR, PTX-ss-BBR NPs and PTX. The cell apoptosis and cell cycle assays indicated that PTX-ss-BBR NPs were conducive to the entry of BBR and PTX into A549 cells and the enhancement of apoptosis effects.

Figure 6

Fig. 6. (A) *In vitro* cell cycle distribution on A549 cells after applying BBR, PTX-ss-BBR NPs and PTX by flow cytometry. (B) G2/M phase rates of A549 cells. Data are presented as the mean ± SD (n=3). $^{#}P < 0.05$ *vs.* Control; $^{###}P < 0.001$ *vs.* Control; $^{**}P < 0.01$ *vs.* BBR; $^{Δ}P < 0.05$ *vs.* PTX-ss-BBR NPs.

3.9. Co-localization in the mitochondria of PTX-ss-BBR NPs

Mitotracker Red was used as a fluorescent probe to evaluate the capacity of the mitochondria target of PTX-ss-BBR NPs. CLSM was employed to observed the mitochondria localization of NPs using A549 cells cultured at 37 ^{o}C for 1h and 2h, respectively. The yellow fluorescence produced by the overlap of green fluorescence and red fluorescence suggested that the chemical achieved mitochondria targeted localization. As shown in Fig. 7, both BBR and NPs were observed with significant green fluorescence that predominantly localized in mitochondria stained as red fluorescence by Mitotracker Red and the fluorescence intensity increased in a time-dependent manner for PTX-ss-BBR NPs with a high Pearson's coefficient (0.91 for Fig. 8A4, 0.94 for Fig. 8B4, 0.98 for Fig. 8C4), suggesting its efficient co-localization in the mitochondria of A549 cells.

Figure 7

Fig. 7. Mitochondria targeting of the BBR and PTX-ss-BBR NPs in A549 cells. The cells in (A1, B1, C1) the green channel, (A2, B2, C2) the red channel and (A3, B3, C3) the merged image were co-loaded with BBR or PTX-ss-BBR NPs with Mitotracker. (A4) The intensity profile of the linear regions of interest across the cell (white line in (A3)). (B4) The intensity profile of the linear regions of interest across the cell (white line in (B3)). (C4) The intensity profile of the linear regions of interest across the cell (white line in (C3)). Green channel: λ_{EX} = 405 nm, λ_{EM} =

500–600 nm; red channel: λ_{EX} = 561 nm, λ_{EM} = 580–660 nm.

3.10. Mitochondrial membrane potential (Δψm)

The energy produced by respiration on the mitochondrial inner membrane drives protons through the inner mitochondrial membrane while establishing mitochondrial membrane potential (Δψm), which is essential for many biological functions of cells, and its alteration activates the apoptotic pathway of the cell [39]. JC-1, a lipophilic cationic dye, is capable of selectively accumulating in the matrix of mitochondria and it will shift from red J-aggregates to green monomers when the mitochondrial electrochemical gradient is destructed. As indicated in Fig. 8, compared to the control group, A549 cells treated with BBR, PTX-ss-BBR NPs and PTX exhibited obviously decreased Δψm. In contrast, the loss of Δψm of PTX-ss-BBR NPs was the most significant, which was almost 1.36-times and 2.14-times higher than that of the BBR and PTX.

Figure 8

Fig. 8. (A) Changes in the mitochondrial membrane potential measured by flow cytometry in A549 cells after treatment with BBR, PTX-ss-BBR NPs and PTX. (B) Quantitative ratio of decreased mitochondrial membrane potential (Δψ). Data are presented as the mean ± SD (n=3). $^{**}P < 0.01$ *vs.* BBR; $^{###}P < 0.001$ *vs.* PTX.

3.11. ROS production

ROS is obligate in maintaining redox homeostasis in cells. Cancer cells are more sensitive to high contents of ROS than normal cells and enhanced intracellular ROS elicits cell death by damaging mitochondrial membrane [40,41]. 2,7-Dichlorofluorescein diacetate (DCFH-DA) is a cell-permeant fluorescent probe, which is employed for visualizing ROS level. As shown in Fig. 9, BBR and PTX-ss-BBR NPs exerted pronounced increase in the fluorescence intensity of 2,7-dichlorofluorescein (DCF) after 48 h treatment with BBR and PTX-ss-BBR NPs in A549 cells by comparison to the control groups and PTX, maybe due to its higher mitochondrial accumulation.

Figure 9

Fig. 9. (A) Intracellular ROS generation measured by flow cytometry in A549 cells after treatment with BBR, PTX-ss-BBR NPs and PTX. (B) Quantitative ratio of mean fluorescent intensity of ROS. Data are presented as the mean ± SD (n=3). $^{#}P < 0.05$ *vs.* Control; $^{###}P < 0.001$ *vs.* Control; $^{*}P < 0.05$ *vs.* BBR; $^{ΔΔ}P < 0.01$ *vs.* PTX-ss-BBR NPs.

4. discussion

In addition to providing the energy necessary for cellular metabolism, mitochondria are also associated with mitochondria in the occurrence of multidrug resistance to many chemotherapeutic

drugs, thus transporting the chemotherapeutic drug to mitochondria are expected to address the resistance of chemotherapy drugs. Considering the excellent mitochondria-targeting feature, antibacterial activity and potential synergetic anticancer effect of BBR and the clinically outstanding contribution of PTX, our work described herein a new GSH-responsive conjugate, which was constructed through a disulfide bond spacer to connect PTX with BBR.

The prepared PTX-ss-BBR NPs had a particle size of about 165 nm, which was relatively stable, and had a prominent GSH-responsible characteristic in the environment of the tumor compared to the normal environment, and contributed to the rapid release of the drug in cancer cells. Molecular simulations revealed that the main driving forces for the formation of nanoparticles were hydrophobic interactions and π-π stacking, which provided theoretical guidance for the development of new self-assembling nanodrugs.

The results of cytotoxicity showed that the PTX-ss-BBR NPs had better anticancer activity, especially against A549 cells. After 48 hours of treatment, the inhibition effect of cancer cells was 20% higher than that of PTX, which might be due to the rapid release of PTX by the PTX-ss-BBR NPs in A549 cells and the synergistic anticancer effect of BBR. Therefore, the biological evaluation by PTX-ss-BBR NPs is worthy of further study. Some researches had found that more than 50% lung cancers are caused by bacterial infections [37, 38]. We also studied the ability of the PTX-ss-BBR NPs to inhibit common lung bacteria, and it was found to have a better activity than BBR against *Staphylococcus aureus* with an MIC value of 4 μM, which provided a new potential for the treatment of lung cancer with bacterial infection.

PTX-ss-BBR NPs could promote apoptosis of cancer cells, which might be due to the action of BBR and PTX on mitochondria. To further investigate the possible mitochondrial mechanisms of nanoparticles, we conducted mitochondrial-related studies. The experimental results found that PTX-ss-BBR NPs could be targeted for delivery to mitochondria and was time dependent. The nanoparticles promoted a decrease in mitochondrial membrane potential and production of reactive oxygen species. In addition, the nanoparticles could also arrest cancer cells in the G2/M phase.

5. Conclusion

In summary, we developed a mitochondria-targeting nanoparticles (PTX-ss-BBR NPs) which were formed through hydrophobic interactions and π−π stacking, as being revealed and verified by using MD simulations. The prepared nanoplatform was sensitive to tumor microenvironment and was imparted the ability for controlled release of drugs. Moreover, PTX-ss-BBR NPs accumulated in the mitochondria of A549 cells *via* charge and lipocationic properties at BBR moiety. The *in vitro* anticancer potency of PTX-ss-BBR NPs on A549 cells was enhanced due to upregulated ROS levels, dissipated mitochondria membrane potential. We also confirmed that PTX-ss-BBR NPs exerted comparable efficacy to BBR against bacteria closely associated with the development

of lung cancer. The synergistic effect of PTX and BBR improved the treatment effect of conventional chemotherapy drugs against A549 cells.

Acknowledgement

The authors gratefully acknowledge the financial support for this research from the National Natural Science Foundation of China (Grant No.: 21606043, 21776046), the Six Talent Peaks Project in Jiangsu Province (Grant No.: XCL-079), the Fundamental Research Funds for the Central Universities (Grant No.: 2242019K40145), and the Recruitment Program for Young Professionals (the Thousand Youth Talents Plan).

References

[1] Y.J. Ko, W.J. Kim, K. Kim, I.C. Kwon, Advances in the strategies for designing receptor-targeted molecular imaging probes for cancer research, J. Control. Release 305 (2019) 1-17.

[2] S.G. Ingle, R.V. Pai, J.D. Monpara, P.R. Vavia, Liposils: An effecuve strategy for stabilizing Paclitaxel loaded liposomes by surface coating with silica, Eur. J. Pharm. Sci. 122 (2018) 51-63.

[3] F. Wang, M. Porter, A. Konstantopoulos, P. Zhang, H. Cui, Preclinical development of drug delivery systems for paclitaxel-based cancer chemotherapy, J. Control. Release 267 (2017) 100-118.

[4] P. Ma, J. Chen, X. Bi, Z. Li, X. Gao, H. Li, H. Zhu, Y. Huang, J. Qi, Y. Zhang, Overcoming multidrug resistance through the glut1-mediated and enzyme-triggered mitochondrial targeting conjugate with redox-sensitive paclitaxel release, ACS Appl. Mater. Interfaces 10 (2018) 12351-12363.

[5] C.P. Liu, C.Y. Xie, J.X. Zhao, K.L. Yu, Y.X. Lei, H. Sun, L.G. Lou, J.M. Yue, Dysoxylactam A: A macrocyclolipopeptide reverses P-glycoprotein-mediated multidrug resistance in cancer cells, J. Am. Chem. Soc. 141 (2019) 6812-6816.

[6] Y. Li, J. Dang, Q. Liang, L. Yu, Thermal-responsive carbon monoxide (CO) delivery expedites metabolic exhaustion of cancer cells toward reversal of chemotherapy resistance, ACS Central Sci. 5 (2019) 1044-1058.

[7] J. Sun, L. Jiang, Y. Lin, E.M. Gerhard, X. Jiang, L. Li, J. Yang, Z. Gu, Enhanced anticancer efficacy of paclitaxel through multistage tumor-targeting liposomes modified with RGD and KLA peptides, Int. J. Nanomed. 12 (2017) 1517-1537.

[8] L. Ruan, M. Zhou, J. Chen, H. Huang, J. Zhang, H. Sun, Z. Chai, Y. Hu, Thermoresponsive drug delivery to mitochondria in vivo, Chem. Commun. (2019) doi: 10.1039/C9CC07538K.

[9] L. Jiang, L. Li, X. He, Q. Yi, B. He, J. Cao, W. Pan, Z. Gu, Overcoming drug-resistant lung cancer by paclitaxel loaded dual-functional liposomes with mitochondria targeting and pH-response, Biomaterials 52 (2015) 126-139.

[10] H. Chen, J. Wang, X. Feng, M. Zhu, S. Hoffmann, A. Hsu, K. Qian, D. Huang, F. Zhao, W. Liu, H. Zhang, Z. Cheng, Mitochondria-targeting fluorescent molecules for high efficiency cancer growth inhibition and imaging, Chem. Sci. 10 (2019) 7946-7951.

[11] S.R. Jean, M. Ahmed, E.K. Lei, S.P. Wisnovsky, S.O. Kelley, Peptide-mediated delivery of chemical probes and therapeutics to mitochondria, Acc. Chem. Res. 49 (2016) 1893-1902.

[12] V. Reshetnikov, S. Daum, C. Janko, W. Karawacka, R. Tietze, C. Alexiou, S. Paryzhak, T. Dumych, R. Bilyy, P. Tripal, B. Schmid, R. Palmisano, A. Mokhir, ROS-responsive N-alkylaminoferrocenes for cancer-cell-specific targeting of mitochondria, Angew. Chem. Int. Edit. 57 (2018) 11943-11946.

[13] T. Li, P. Wang, W. Guo, X. Huang, X. Tian, G. Wu, B. Xu, F. Li, C. Yan, X. Liang, H. Lei, Natural berberine-based chinese herb medicine assembled nanostructures with modified antibacterial application, ACS Nano 13 (2019) 6770-6781.

[14] A. Luganini, B. Mercorelli, L. Messa, G. Palu, G. Gribaudo, A. Loregian, The isoquinoline alkaloid berberine inhibits human cytomegalovirus replication by interfering with the viral immediate early-2 (IE2) protein transactivating activity, Antivir. Res. 164 (2019) 52-60.

[15] J. Yin, Y. Hou, Y. Yin, X. Song, Selenium-coated nanostructured lipid carriers used for oral delivery of berberine to accomplish a synergic hypoglycemic effect, Int. J. Nanomed. 12 (2017) 8671-8680.

[16] L. Tan, Y. Wang, G. Ai, C. Luo, H. Chen, C. Li, H. Zeng, J. Xie, J. Chen, Z. Su, Dihydroberberine, a hydrogenated derivative of berberine firstly identified in phellodendri chinese cortex, exerts anti-inflammatory effect via dual modulation of NF-κB and MAPK signaling pathways, Int. Immunopharmacol. 75 (2019) 105802.

[17] J. Song, C. Lin, X. Yang, Y. Xie, P. Pu, H. Li, W. Zhu, H. Hu, Mitochondrial targeting nanodrugs self-assembled from 9-O-octadecyl substituted berberine derivative for cancer treatment by inducing mitochondrial apoptosis pathways, J. Control. Release 294 (2019) 27-42.

[18] S. Fu, Y. Xie, J. Tuo, Y. Wang, W. Zhu, S. Wu, G. Yan, H. Hu, Discovery of mitochondria-targeting berberine derivatives as the inhibitors of proliferation, invasion and migration against rat C6 and human U87 glioma cells, Med. Chem. Commun., 6 (2015) 164.

[19] J. Tuo, Y. Xie, J. Song, Y. Chen, Q. Guo, X. Liu, X. Ni, D. Xu, H. Huang, S. Yin, W. Zhu, J. Wu, H. Hu, Development of a novel berberine-mediated mitochondria-targeting nano-platform for drug-resistant cancer therapy, J. Mater. Chem. B 4 (2016) 6856.

[20] C.V. Diogo, N.G. Machado, I.A. Barbosa, T.L. Serafim, A. Burgeiro, P.J. Oliveira, Berberine as a promising safe anti-cancer agent-is there a role for mitochondria? Current Drug Targets 12 (2011) 850-859.

[21] R. An, Z. Gu, H. Sun, Y. Hu, R. Yan, D. Ye, H. Liu, Self-assembly of fluorescent dehydroberberine enhances mitochondria-dependent antitumor efficacy, Chem. Eur. J. 24 (2018) 9812-9819.

[22] Z.H. Zhou, Y. Piao, L.Q. Hao, G.Y. Wang, Z.X. Zhou, Y.Q. Shen, Acidity-responsive shell-sheddable camptothecin-based nanofibers for carrier-free cancer drug delivery, Nanoscale 11 (2019) 15907.

[23] G. Yang, S.Z.F. Phua, A.K. Bindra, Y. Zhao, Degradability and clearance of inorganic nanoparticles for biomedical applications, Adv. Mater. 31 (2019) 1805730.

[24] Z. Zhang, Y.H. Ji, Mesoporous manganese dioxide coated gold nanorods as a multiresponsive nanoplatform for drug delivery, Ind. Eng. Chem. Res. 58 (2019) 2991-2999.

[25] Y. Cheng, Y.H. Ji, RGD-modified polymer and liposome nanovehicles: Recent research progress for drug

delivery in cancer therapeutics, Eur. J. Pharm. Sci. 128 (2019) 8-17.

[26] F. Man, P.J. Gawne, R.T.M. de Rosales, Nuclear imaging of liposomal drug delivery systems: A critical review of radiolabelling methods and applications in nanomedicine, Adv. Drug Deliver. Rev. (2019) doi: 10.1016/j.addr.2019.05.012.

[27] Z. Chen, Z. Wang, Z. Gu, Bioinspired and biomimetic nanomedicines, Acc. Chem. Res. 52 (2019) 1255-1264.

[28] I.O. Lebedeva, E.B. Zhulina, O.V. Borisov, Self-assembly of linear-dendritic and double dendritic block copolymers: From dendromicelles to dendrimersomes, Macromolecules 52 (2019) 3655-3667.

[29] Y. Yang, C. Yue, Y. Han, W. Zhang, A. He, C. Zhang, T. Yin, Q. Zhang, J. Zhang, Y. Yang, J. Ni, J. Sun, D. Cui, Adv. Funct. Mater. 26 (2016) 8735-8745.

[30] X. Zheng, Z. Li, L. Chen, Z. Xie, X. Jing, Self-assembly of porphyrin-paclitaxel conjugates into nanomedicines: enhanced cytotoxicity due to endosomal escape, Chem. Asian J. 11 (2016) 1780-1784.

[31] G. Lin, L. Li, N. Panwar, J. Wang, S.C. Tjin, X. Wang, K.T. Yong, Non-viral gene therapy using multifunctional nanoparticles: Status, challenges, and opportunities, Coordin. Chem. Rev. 374 (2018) 133-152.

[32] W. He, X. Hu, W. Jiang, R. Liu, D. Zhang, J. Zheng, Z. Li, Y. Luan, Rational design of a new self-codelivery system from redox-sensitive camptothecin-cytarabine conjugate assembly for effectively synergistic anticancer therapy, Adv. Healthcare Mater. 6 (2017) 1700829.

[33] Y. Wang, T. Zhang, C. Hou, M. Zu, Y. Lu, X. Ma, Die Jia, P. Xue, Y. Kang, Z. Xu, Mitochondria-specific anticancer drug delivery based on reductive-activated polyprodrug for enhancing the therapeutic effect of breast cancer chemotherapy, ACS Appl. Mater. Interfaces (2019) doi: 10.1021/acsami.9b10211.

[34] J. Peng, Q. Yang, Y. Xiao, K. Shi, Q. Liu, Y. Hao, F. Yang, R. Han, Z. Qian, Tumor microenvironment responsive drug-dye-peptide nanoassembly for enhanced tumor-targeting, penetration, and photo-chemo-immunotherapy, Adv. Funct. Mater. 29 (2019) 1900004.

[35] D. Shivakumar, J. Williams, Y. Wu, W. Damm, J. Shelley, W. Sherman, Prediction of absolute solvation free energies using molecular dynamics free energy perturbation and the OPLS force field, J. Chem. Theory Comput. 6 (2010) 1509-1519.

[36] N. Gong, X. Ma, X. Ye, Q. Zhou, X. Chen, X. Tan, S. Yao, S. Huo, T. Zhang, S. Chen, X. Teng, X. Hu, J. Yu, Y. Gan, H. Jiang, J. Li, X. Liang, Carbon-dot-supported atomically dispersed gold as a mitochondrial oxidative stress amplifier for cancer treatment, Nat. Nanotechnol. 14 (2019) 379-387.

[37] C. Jin, G.K. Lagoudas, C. Zhao, S. Bullman, A. Bhutkar, B. Hu, S. Ameh, D. Sandel, X.S. Liang, S. Mazzilli, M.T. Whary, M. Meyerson, R. Germain, P.C. Blainey, J.G. Fox, T. Jacks, Commensal microbiota promote lung cancer development via γδ T cells, Cell 176 (2019) 998-1013.

[38] K.S. Akinosoglou, K. Karkoulias, M. Marangos, Infectious complications in patients with lung cancer, Eur. Rev. Med. Pharmaco. 17 (2013) 8-18.

[39] M. Tian, Y. Ma, W. Lin, Fluorescent Probes for the Visualization of Cell Viability, Acc. Chem. Res. 52 (2019) 2147-2157.

[40] B. Yang, H. Liu, H. Yan, W. Chen, J. Wu, X. Feng, R. Tong, H. Yu, Y. Chen, Z. Lv, W. Sun, B. He, J. Wu, G. Yu, Z. Mao, S. Zheng, Combinatorial photochemotherapy on liver cancer stem cells with organoplatinum(II) metallacage-based nanoparticles, J. Mater. Chem. B (2019) doi: 10.1039/c9tb01299k.

[41] C. Xu, Y. Sun, Y. Qi, Y. Yu, Y. He, M. Hu, Q. Hu, T. Wu, D. Zhang, L. Shang, H. Deng, Z. Zhang, Selective self-induced stimulus amplification prodrug platform for inhibiting multidrug resistance and lung metastasis, J. Control. Release 284 (2018) 224-239.

Lists of tables, figures and schemes captions

Scheme 1 Synthetic route of GSH-responsive PTX-ss-BBR conjugate.

Fig. 1. (A) TEM image of PTX-ss-BBR NPs. (B) TEM image of PTX-ss-BBR NPs treated with 10 mM GSH for 6h. (C) Particle size of PTX-ss-BBR NPs. (D) Changes of diameter of PTX-ss-BBR nanoparticles in PBS or in PBS and FBS for 3 days. (E) *In virto* release kinetics of drug from NPs in pH 7.4 PBS with or without GSH. (F) The light scattering intensities (Kcps) of acquous solutions containing varying concentration PTX-ss-BBR conjugates.

Fig. 2. The supramolecular assembly process of PTX-ss-BBR conjugate in water by MD simulations.

Fig. 3. (A) The solvent accessible surface areas of the assembled nanostructures and the number of hydrogen bonds between the cluster and water. (B) Solvation free energy of assembled nanostructures.

Fig. 4. *In vitro* anticancer activity of self-assembled PTX-ss-BBR NPs, PTX and BBR against A549 cells for 24h (A) or 48h (B), HeLa cells for 24h (C) or 48h (D), HepG2 cells for 24h (E) or 48h (F). Data are presented as the mean ± SD (n=3). $^{*}P < 0.05$ *vs.* PTX; $^{\#}P < 0.05$ *vs.* BBR; $^{\#\#}P < 0.01$ *vs.* BBR; $^{\#\#\#}P < 0.001$ *vs.* BBR.

Table 1 IC_{50} values of free BBR, PTX and PTX-ss-BBR NPs on A549, HeLa and HepG2 cells at different times.

Table 2 *In vitro* antibacterial activity data as MIC (μM) for PTX-ss-BBR NPs and BBR against *S. aureus, S. pneumonia* and *E. coli*.

Fig. 5. (A) *In vitro* apoptosis analysis against A549 cells treated by BBR, PTX-ss-BBR NPs, and PTX and analyzed by Annexin-V-FITC/PI double staining method. (B) Quantitative ratio of apoptosis. Data are presented as the mean ± SD (n=3). $^{\#\#\#}P < 0.001$ *vs.* Control; $^{***}P < 0.001$ *vs.* BBR; $^{***}P < 0.001$ *vs.* PTX.

Fig. 6. (A) *In vitro* cell cycle distribution on A549 cells after applying BBR, PTX-ss-BBR NPs and PTX by flow cytometry. (B) G2/M phase rates of A549 cells. Data are presented as the mean ± SD (n=3). $^{\#}P < 0.05$ *vs.* Control; $^{\#\#\#}P < 0.001$ *vs.* Control; $^{**}P < 0.01$ *vs.* BBR; $^{\Delta}P < 0.05$ *vs.* PTX-ss-BBR NPs.

Fig. 7. Mitochondria targeting of the BBR and PTX-ss-BBR NPs in A549 cells. The cells in (A1, B1, C1) the green channel, (A2, B2, C2) the red channel and (A3, B3, C3) the merged image were co-loaded with BBR or PTX-ss-BBR NPs with Mitotracker. (A4) The intensity profile of the linear regions of interest across the cell (white line in (A3)). (B4) The intensity profile of the linear regions of interest across the cell (white line in (B3)). (C4) The intensity profile of the linear regions of interest across the cell (white line in (C3)). Green channel: λ_{EX} = 405 nm, λ_{EM} = 500–600 nm; red channel: λ_{EX} = 561 nm, λ_{EM} = 580–660 nm.

Fig. 8. (A) Changes in the mitochondrial membrane potential measured by flow cytometry in A549 cells after treatment with BBR, PTX-ss-BBR NPs and PTX. (B) Quantitative ratio of decreased mitochondrial membrane potential ($\Delta\psi$). Data are presented as the mean ± SD (n=3). $^{**}P < 0.01$ *vs.* BBR; $^{###}P < 0.001$ *vs.* PTX.

Fig. 9. (A) Intracellular ROS generation measured by flow cytometry in A549 cells after treatment with BBR, PTX-ss-BBR NPs and PTX. (B) Quantitative ratio of mean fluorescent intensity of ROS. Data are presented as the mean ± SD (n=3). $^{\#}P < 0.05$ *vs.* Control; $^{###}P < 0.001$ *vs.* Control; $^{*}P < 0.05$ *vs.* BBR; $^{\Delta\Delta}P < 0.01$ *vs.* PTX-ss-BBR NPs.

Table 1 IC_{50} values of free BBR, PTX and PTX-SS-BBR NPs on A549, HeLa and HepG2 cells at different times.

Formulation	IC_{50} (μM) on A549 cells		IC_{50} (μM) on HeLa cells		IC_{50} (μM) on HepG2 cells	
	24 h	48 h	24 h	48 h	24 h	48 h
PTX	1.545±0.232	0.31±0.021	8.876±0.147	1.653±0.117	8.471±0.027	1.936±0.085
BBR	–	28.59±0.352	–	40.18±0.537	–	37.72±0.489
PTX-SS-BBR NPs	1.295±0.132	0.243±0.014	10.573±0.231	1.512±0.201	12.402±0.134	2.515±0.148

Table 2 *In vitro* antibacterial activity data as MIC (μM) for PTX-ss-BBR NPs and BBR against *S. aureus*, *S. pneumonia* and *E. coli*.

Formulation	*S. pneumoniae*	*S. aureus*	*E. coli*
BBR	16	8	8
PTX-ss-BBR NPs	32	4	8

Mitochondria-targeting nanomedicine self-assembled from GSH-responsive paclitaxel-ss-berberine conjugate for synergetic cancer treatment with enhanced cytotoxicity

Yu Cheng, Yuanhui Ji*

Jiangsu Province Hi-Tech Key Laboratory for Biomedical Research, School of Chemistry and Chemical Engineering, Southeast University, Nanjing, 211189, P.R. China.

* Corresponding author: Tel: +86-13951907361; Email: yuanhui.ji@seu.edu.cn; yuanhuijinj@163.com.

Mitochondria-targeting GSH-sensitive nanoparticles (PTX-ss-BBR NPs) were formed through hydrophobic interactions and π-π stacking. The prepared nanoplatform was sensitive to tumor microenvironment and was imparted the ability for controlled release of drugs. The *in vitro* anticancer potency of PTX-ss-BBR NPs on A549 cells was enhanced due to upregulated ROS levels, dissipated mitochondria membrane potential.

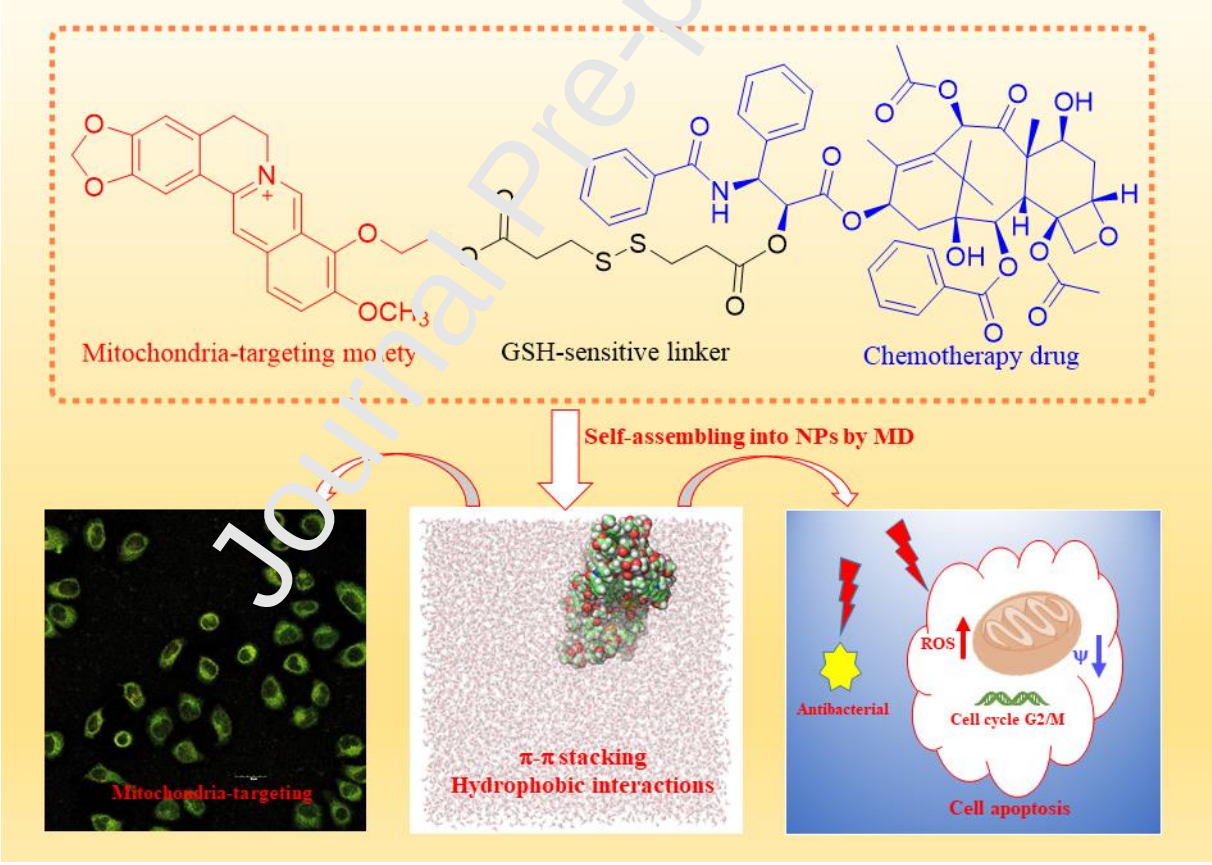

►New mitochondria-targeting PTX-ss-BBR conjugate was developed.

►Computer simulation studies rationalized the self-assembly process of PTX-ss-BBR.

►PTX-ss-BBR NPs exhibited better activity against A549 cells and *S. aureus*.

►PTX-ss-BBR NPs were GSH-sensitive and mitochondria-targeting.

►PTX-ss-BBR NPs can effectively dissipate mitochondrial membrane potential, upregulate ROS levels, arreste cells in phase G2/M.